DOI 10.1007/s11182-020-02054-y
Russian Physics Journal, Vol. 63, No. 3, July, 2020 (Russian Original No. 3, March, 2020)

PHYSICS OF SEMICONDUCTORS AND DIELECTRICS

ADMITTANCE OF BARRIER STRUCTURES BASED ON MERCURY CADMIUM TELLURIDE

A. V. Voitsekhovskii,[1] S. N. Nesmelov,[1] S. M. Dzyadukh,[1] S. A. Dvoretsky,[1,2] N. N. Mikhailov,[2] G. Yu. Sidorov,[2] and M. V. Yakushev[2]

UDC 621.315.592

The results of studying the admittance of unipolar barrier structures based on HgCdTe *grown by molecular beam epitaxy (MBE) on* GaAs *(013) substrates are presented. Using passivation with an* Al_2O_3 *insulator, device nBn structures based on* HgCdTe *were fabricated. The layer parameters in the created structures provided the possibility of detection in the spectral range of 3–5 μm. Based on the analysis of the frequency dependences of the admittance, an equivalent circuit of nBn structures at small biases is proposed. The dependences of the equivalent circuit parameters on the area of the mesa structure and temperature are determined. The properties of high-temperature maxima in the voltage dependences of the capacitance and conductance of nBn structures, which are presumably related to the recharging of surface states at the heterointerface between the barrier and absorbing layers, are studied. It is found that in a wide range of frequencies and temperatures, the capacitance – voltage characteristics of nBn structures based on* HgCdTe *at reverse biases can be used to determine the concentration of donor impurities in the absorbing layer. It is shown that the admittance of test MIS devices in a mesa configuration, formed on the basis of the MBE* HgCdTe *nBn structures, is determined by the combined influence of electronic processes in the contact, barrier, and absorbing layers.*

Keywords: HgCdTe, molecular beam epitaxy, *nBn* structure, barrier detectors, admittance, capacitance-voltage characteristic, equivalent circuit method, impurity concentration.

INTRODUCTION

The fundamental properties of the semiconductor solid solutions of mercury cadmium telluride (HgCdTe, $Hg_{1-x}Cd_xTe$) are well suited to create highly sensitive infrared detectors based on this material for spectral regions of 3–5 and 8–12 μm (MWIR and LWIR, respectively) [1, 2]. Further progress in HgCdTe-based infrared detectors is restrained by the quality of the material and the need for significant cooling of detectors to suppress the thermal components of the dark current. Device-grade HgCdTe films are currently produced by molecular beam epitaxy (MBE), as well as by metal organic chemical vapor deposition (MOCVD).

One of the technological problems that arise when creating arrays of photodiodes based on MBE HgCdTe is the defect formation during the creation of p – n-junctions by ion implantation and concomitant annealings [3, 4]. Possibilities to exclude the procedure of ion implantation from the technological cycle of creating photosensitive

[1]National Research Tomsk State University, Tomsk, Russia, e-mail: vav43@mail.tsu.ru; nesm69@mail.ru; bonespirit@mail2000.ru; [2]Rzhanov Institute of Semiconductor Physics of the Siberian Branch of the Russian Academy of Sciences, Novosibirsk, Russia, e-mail: dvor@isp.nsc.ru; mikhailov@isp.nsc.ru; george@isp.nsc.ru; yakushev@isp.nsc.ru. Translated from Izvestiya Vysshikh Uchebnykh Zavedenii, Fizika, No. 3, pp. 76–87, March, 2020. Original article submitted January 10, 2020.

elements based on MBE HgCdTe are provided by the development of unipolar barrier detectors in which all layers have an electronic type of conductivity. As such detectors, *nBn* structures can be used in which relatively narrow-gap layers of the *n*-type material (the contact and absorbing layers) are separated by a wide-gap barrier of the electronic type of conductivity. Such structures, the concept of which was first proposed in 1983 [5], can be considered as high impedance photoresistors [1].

The optimal characteristics of *nBn* detectors can be realized at a small (close to zero) value of the barrier height in the valence band, which is difficult to implement using standard materials for infrared detection, such as InSb and HgCdTe. The situation radically changed in the middle of the first decade of the 21st century in connection with the studies of properties of the family of the group (III – V) materials with a lattice constant of 6.1 Å and the creation of the first barrier detectors based on these materials [6, 7]. Currently, based on InAs and InAsSb, barrier detectors in the *nBn* configuration are being actively developed [8–11].

A significant amount of works has been devoted to theoretical analysis of the characteristics of *nBn* detectors based on HgCdTe (for example, [12–17]), but only a limited number of attempts have been made to implement such detectors in practice [18–22]. The characteristics of previously created *nBn* detectors based on MBE HgCdTe are far from ideal ones [18–20]. Somewhat greater successes were achieved in the creation of *nBn* detectors based on MOCVD HgCdTe [21, 22], but the problem of the defect formation during implantation is not relevant when using this material. MOCVD technology allows one to obtain high-quality *p*-type conductance layers and use such layers to create barriers in *nBn* structures. Recently, the creation of MWIR *nBn* structures based on MBE HgCdTe was reported, in which a diffusion-limited dark current was observed at temperatures from 180 to 300 K [23, 24].

Further studies of processes in *nBn* structures based on MBE HgCdTe open up the possibility of realizing the potential advantages of the MBE technology when creating barrier detectors. The standard approach to studying the properties of the manufactured *nBn* detectors is to measure the current – voltage characteristics at various temperatures, which often makes it possible to establish the dominant mechanisms of dark current. To obtain more detailed information about processes in real structures, it is necessary to use various experimental methods. The admittance method is very informative, which is confirmed by its wide use in studies of semiconductor structures [25–28]. However, only a few works are known devoted to the use of the admittance method in studying the properties of *nBn* structures based on the group III–V materials [10, 29, 30]. Preliminary results of studying the admittance of *nBn* structures based on MBE HgCdTe are presented in [31, 32]. The first studies of the admittance of "planar" MIS devices based on MBE HgCdTe *nBn* structures, in which a backward electrode was deposited onto a contact layer, were also described previously [33]. The studies have shown that the admittance dependences are very sensitive to the features of real *nBn* structures. Therefore, the formation technology of such structures significantly affects the measurement results.

This paper summarizes some results of studies of the admittance of unipolar barrier structures based on MBE HgCdTe. In a wide range of frequencies and temperatures, the electrophysical characteristics of MWIR *nBn* structures based on MBE HgCdTe, in which the dark current is limited by diffusion processes, are studied. The first results of studying the admittance of test MIS devices based on MBE HgCdTe *nBn* structures formed by applying a backward contact to the absorbing layer are presented.

SAMPLES AND MEASUREMENT TECHNIQUES

The *n*-$Hg_{1-x}Cd_xTe$ films for the creation of *nBn* structures were grown by molecular beam epitaxy at the Institute of Semiconductor Physics of SB RAS. The film growth rate was 1.68 μm/h. The following layers were sequentially grown on the top of the GaAs (013) substrate: buffer layers of ZnTe and CdTe and a graded-gap $Hg_{1-x}Cd_xTe$ layer with the composition variation from 0.78 to 0.35. Then, the absorbing, barrier, and contact layers were formed of *n*-$Hg_{1-x}Cd_xTe$. The component composition of the absorbing layer provided the possibility of interband photogeneration in the MWIR range. A schematic representation of the fabricated *nBn* structures is shown in Fig. 1*a*, which also shows the basic parameters of the layers. In the process of growing, the working area was doped with an indium impurity. The donor impurity concentrations in the absorbing and barrier layers were chosen equal. Based on the grown multilayer film, the device *nBn* structures were fabricated. For further deposition of the contact frame, HgCdTe was etched in a 0.5% solution of Br in HBr to the absorbing layer. Mesa structures necessary for the physical

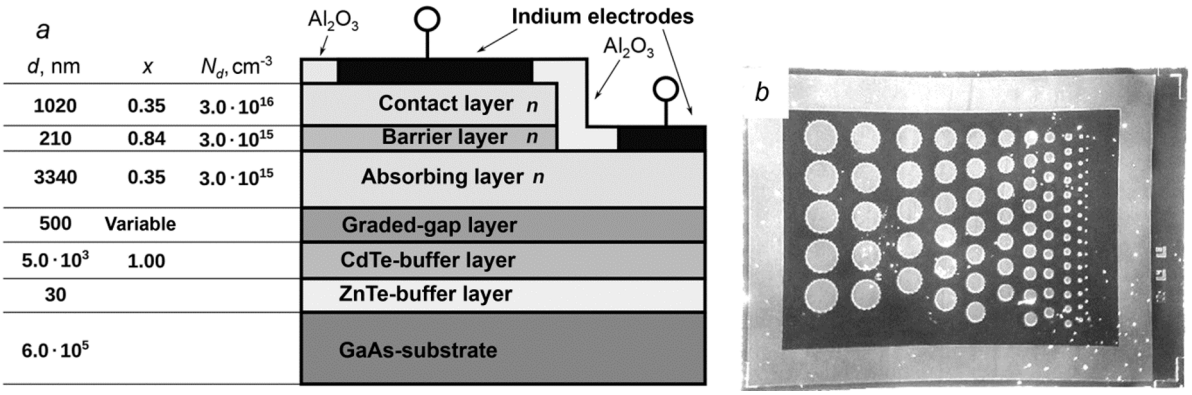

Fig. 1. Schematic representation of the fabricated *nBn* structure based on MBE HgCdTe (*a*) and a photograph of the fabricated sample under study (*b*).

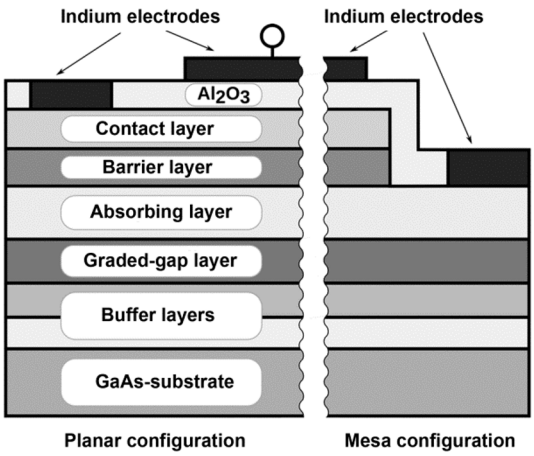

Fig. 2. Schematic representation of MIS devices based on MBE HgCdTe *nBn* structures in a planar configuration (left) and mesa configuration (right).

separation of individual elements (*nBn* structures) were also formed by etching using photolithography. Al_2O_3 films deposited at a temperature of 120°C by plasma atomic layer deposition (PE ALD) were used as a passivating coating [34, 35]. The PE ALD Al_2O_3 insulator films were etched using a mixture of hydrofluoric acid and ammonium fluoride in the region of formation of the contact frame, as well as in the regions of further deposition of frontal electrodes on the contact layer. Indium electrodes were created by thermal spraying at fairly low temperatures (<100°C). The created *nBn* structures had different diameters of mesa structures (from 20 to 500 μm) and frontal electrodes (Fig. 1*b*).

To study the processes in various layers of *nBn* structures, test MIS devices were formed. When creating test MIS devices based on *nBn* structures, no etching was performed to ensure contact with the *nBn* structure, and the front indium electrodes were deposited on the top of the PE ALD Al_2O_3 layer. The backward electrodes were made in two different ways. When creating MIS devices in a planar configuration, no etching was performed, and a contact frame deposited on the contact layer was used as the backward electrode (Fig. 1*b*).

When creating MIS devices in the mesa configuration, etching to the absorbing layer was carried out, and the contact frame was applied to the absorbing layer at the etching sites. The arrangement of the backward electrodes in the planar and mesa MIS structures based on MBE HgCdTe *nBn* structures is shown schematically in Fig. 2.

Admittance measurements were carried out on an automated setup of admittance spectroscopy of nanoheterostructures based on Janis non-optical cryostat, Lake Shore temperature controller, and Agilent E4980A

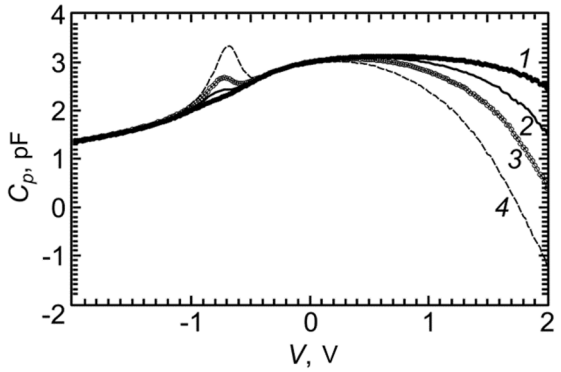

Fig. 3. C–V characteristics of *nBn* structures measured at a frequency of 50 kHz at various temperatures, K: 255 (*1*), 275 (*2*), 290 (*3*), and 310 (*4*).

immittance meter. The measurements of electrical characteristics were carried out in the temperature range 9–300 K at frequencies from 1 kHz to 2 MHz.

To analyze the experimental dependences of admittance, the equivalent circuit method was used [25, 26]. In the admittance measurements, a parallel equivalent circuit was used, i.e., the values of the capacitance C_p and the resistance R_p (or conductance $G_p = 1/R_p$) connected in parallel were determined. The measurement results can be easily converted to a serial circuit consisting of the series-connected capacitance C_s and resistance R_s using the following relationships:

$$C_s = \frac{1+\omega^2 C_p^2 R_p^2}{\omega^2 C_p R_p^2},\ R_s = \frac{R_p}{1+\omega^2 C_p^2 R_p^2}, \tag{1}$$

where ω is the angular frequency ($\omega = 2\pi f$, f is the frequency in Hz). It is easy to write the inverse relations

$$C_p = \frac{C_s}{1+\omega^2 C_s^2 R_s^2},\ R_p = \frac{1+\omega^2 C_s^2 R_s^2}{\omega^2 C_s^2 R_s}. \tag{2}$$

To present the results of the admittance measurements, the conductance of the semiconductor structure normalized to the angular frequency ω is often used $L_p = G_p / \omega$.

EXPERIMENTAL RESULTS AND DISCUSSION

Dependences of the admittance of *nBn* structures based on MBE HgCdTe

Figure 3 shows the capacitance–voltage (C–V) characteristics of an *nBn* structure based on MBE HgCdTe with a mesa diameter of 100 μm measured at a frequency of 50 kHz at various temperatures. At temperatures not exceeding 300 K, the maximum capacitance values are observed at voltages close to 0.3 V. In this case, the barrier layer is completely depleted. With an increase in the reverse (negative) biases, the space charge region (SCR) extends into the depth of the absorbing layer, which leads to a decrease in the capacitance values. At the forward (positive) biases, the capacitance also decreases, and the frequency and temperature dispersions of the voltage dependence are observed. At high temperatures (and low frequencies), the capacitance at forward biases can take negative values. The negative capacitance can occur, if there is a delay in the alternating current changes relative to the alternating test voltage. Possible causes of the current inertia in semiconductor structures are discussed, for example, in [36–38]. At sufficiently high temperatures (>260 K) and voltages of about –0.7 V, a maximum is observed in the C–V characteristic, whose

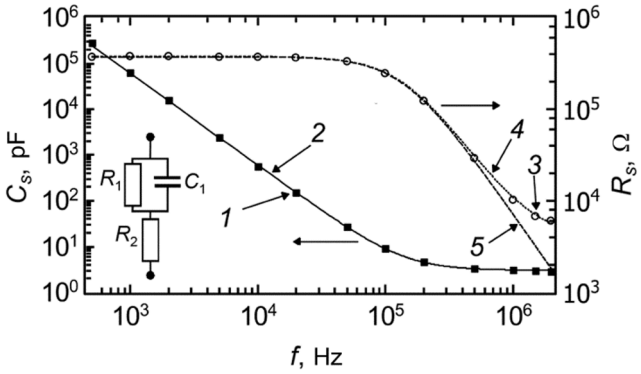

Fig. 4. Experimental (curves *1*, *2*, and symbols) and calculated (curves *3*, *4*, and lines) dependences of the capacitance C_s (curves *1*, *3*,) and resistance R_s (curves *2*, *4*) of the *nBn* structure on the frequency *f* at a temperature of 300 K and a voltage of 0.3 V, as well as the calculated dependence of the resistance (curve *5*, line) on the frequency at R_2= 0. The inset shows the equivalent circuit of the *nBn* structure at voltages close to zero.

amplitude increases with decreasing frequency. The differential conductance of the *nBn* structure is maximum at positive voltages, when the current through the structure is maximum.

The symbols in Fig. 4 show the experimental frequency dependences of the capacitance C_s and resistance R_s of the *nBn* structure measured at a temperature of 300 K and a voltage of 0.3 V. To calculate the frequency dependences, we used the equivalent circuit shown in the inset in Fig. 4. In this circuit, the elements R_1 and C_1 characterize the properties of the barrier layer, and the resistance R_2 characterizes the properties of the absorbing layer bulk. Using expressions (1), for the values of R_s and C_s, we can write

$$R_s = \frac{R_1}{1+\omega^2 C_1^2 R_1^2} + R_2\,,\; C_s = \frac{1+\omega^2 C_1^2 R_1^2}{\omega^2 C_1 R_1^2}\,. \tag{3}$$

It follows from expressions (3) that the capacitance values C_s are independent of R_2. When the condition $\omega^2 C_1^2 R_1^2 >> 1$ is fulfilled, the equalities $C_s = C_1$ and $R_s = R_2$ are fulfilled. Figure 4 shows that the experimental frequency dependences of the *nBn* structure admittance are in good agreement with the calculation results at R_1 = 373.5 kΩ, C_1 = 3.054 pF, and R_2 = 3870 Ω. Without taking into account the resistance of the absorbing layer, noticeable differences in the experimental and calculated dependences of the resistance R_s at high frequencies are observed (curve *5* in Fig. 4).

Dependences of the equivalent circuit elements of *nBn* structures on the mesa structure area and temperature

Figure 5 shows the dependences of the values of the circuit elements on the mesa structure area (*A*) in logarithmic coordinates found from the frequency dependences of the admittance measured at a temperature of 300 K and a voltage of 0.3 V. The capacitance of the barrier layer C_1 increases linearly with increasing area of the structure, and the values of the resistance of the barrier layer R_1 are inversely proportional to the area of the structure. The values of the absorbing layer resistance R_2 do not show a clear dependence on the area of the structure. Figure 6 shows the temperature dependences of the values of the resistances R_1 and R_2 measured at a voltage of 0.3 V for the structure with the diameter of 100 μm. It can be seen that the resistance of the barrier R_1 sharply increases upon cooling and it is difficult to determine the values of this resistance at low temperatures (<220 K). The resistance of the absorbing layer R_2 is weakly and non-monotonically dependent on temperature.

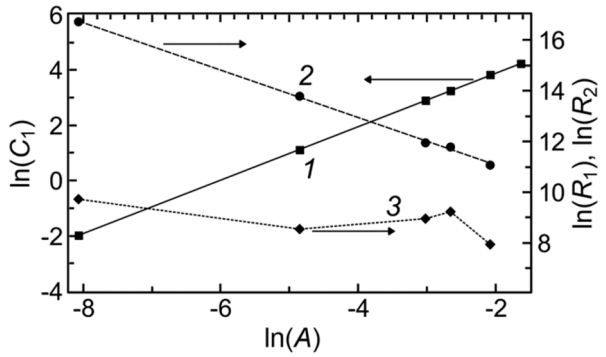

Fig. 5

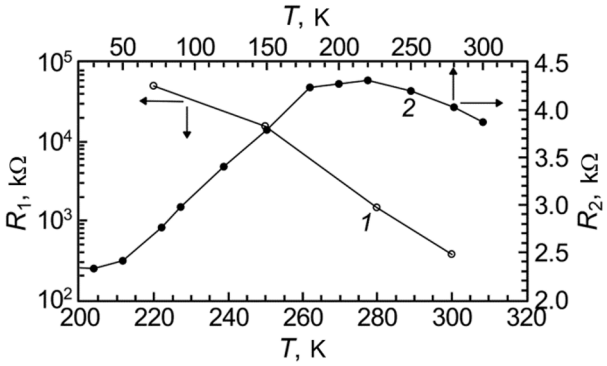

Fig. 6

Fig. 5. Experimental dependences of the values of the elements C_1 (*1*), R_1 (*2*), and R_2 (*3*) on the area of the mesa structure A in logarithmic coordinates at a voltage of 0.3 V and a temperature of 300 K, as well as linear approximations for the dependences C_1 and R_1.

Fig. 6. Temperature dependences of the values of the elements R_1 (*1*) and R_2 (*2*) for an *nBn* structure with the diameter of 100 μm at a voltage of 0.3 V.

With an increase in temperature from 10 to 200 K, the resistance R_2 slightly increases due to a decrease in the electron mobility. With an increase in temperature from 220 to 300 K, it slightly decreases due to an increase in the contribution of the minority carriers (holes) conductance to the total conductance. The temperature dependence of the resistance R_2 found in studies of the *nBn* structure admittance is in good agreement with the similar dependence of the absorbing layer resistance measured when two contacts were created on the absorbing layer. The dependence $R_2(T)$ is qualitatively similar to the temperature dependence of the series bulk resistance of an *n*-HgCdTe epitaxial film, which was previously found from MIS measurements [39–41].

Concentration of donor impurity in the absorbing layer

The concentration of doping impurity in the near-surface region of the absorbing layer, as well as the dependence of the impurity concentration on the coordinate near the heterointerface between the barrier and the absorbing layer, can be determined from the voltage dependence of the capacitance at reverse (negative) biases [42]. For the concentration of donor impurity, one can write the following expression [29]:

$$N_d = \frac{2}{\varepsilon_s \varepsilon_0 q \dfrac{d(C_A^{-2})}{dV}},$$

where ε_s is the relative permittivity of the absorbing layer, ε_0 is the permittivity of vacuum, q is the electron charge, V is the bias voltage, $C_A = \dfrac{C_p}{A}$ is the capacitance of the *nBn* structure per unit area, F/m^2.

Figure 7 shows the C–V characteristics at reverse biases and the $C_A^{-2}(V)$ dependences measured at a temperature of 220 K for *nBn* structures with different diameters. It can be seen that the experimental $C_A^{-2}(V)$ dependences are well approximated by the straight lines, which indicates a uniform distribution of indium concentration over the thickness of the absorbing layer. The found integral concentrations of the dopant were $4.97 \cdot 10^{21}$, $4.73 \cdot 10^{21}$, and

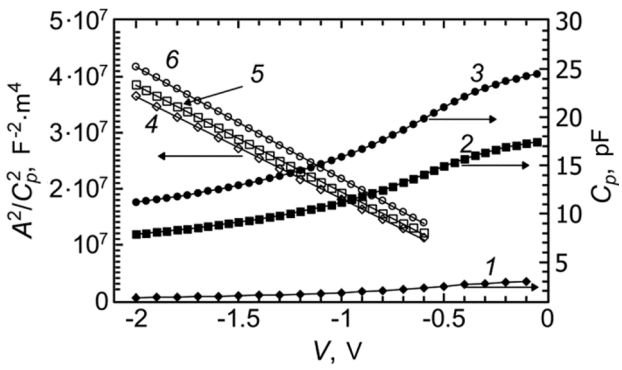

Fig. 7

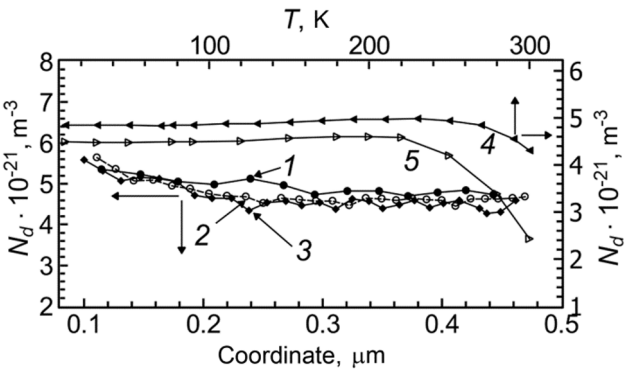

Fig. 8

Fig. 7. C–V characteristics (*1–3*) and voltage dependences of A^2/C_p^2 (*4–6*) at a temperature of 220 K for *nBn* structures with the diameters, μm: 100 (*1*, *4*), 250 (*2*, *5*), and 300 (*3*, *6*).

Fig. 8. Dependences of the donor impurity concentration N_d on the coordinate at a temperature of 220 K, as well as the temperature dependences of the integral concentration N_d found from the measurements of admittance at a frequency of 100 kHz for *nBn* structures with the diameters, μm: 100 (*1*, *4*), 250 (*2*), and 300 (*3*, *5*).

$4.52 \cdot 10^{21}$ m^{-3} for the mesa structure diameters of 100, 250, and 300 μm, respectively. Figure 8 shows the temperature dependences of the integral dopant concentration. It can be seen that the determined concentration N_d is practically independent of temperature in the range from 10 to 220 K. With further heating, the determined concentration decreases which is associated with high-temperature distortions of the C–V characteristic. These distortions are likely due to the recharging of levels located near the heterointerface (which is discussed below). The possibilities of determining the concentration of donor impurity by the admittance measurements at various frequencies were also studied. With an increase in frequency from 2 to 500 kHz, the determined concentration decreased by less than 6%. This is due to the high-frequency effect of the resistance of the absorbing layer bulk on the measured C–V characteristics. Figure 8 also shows the dependences of the dopant concentration on the coordinate in the absorbing layer for *nBn* structures with different mesa diameters (the coordinate is counted off from the heterointerface between the absorbing and barrier layers). With distance from the heterointerface into the depth of the absorbing layer, the impurity concentration decreases slightly.

A similar technique cannot be used to determine the impurity concentration in the contact layer, since at forward biases, the distortion of the C–V characteristics is observed due to the large current flowing through the *nBn* structure, which manifests itself in the frequency dispersion and even negative capacitance values. The impurity concentration in the contact layer can be found from the admittance measurements of the test MIS structures [33].

High-temperature maxima in the voltage dependences of the capacitance and conductance of *nBn* structures

It can be noted that the admittance method is very sensitive to the formation technology of *nBn* structures, since defects at the heterointerfaces and in the adjacent regions of the semiconductor affect the measurement results. It was previously noted that the C–V characteristics of *nBn* structures at high temperatures and low frequencies show a maximum at reverse biases, which does not allow one to correctly determine the dopant concentration at high temperatures. In the frequency dependences of the *nBn* structure conductance, a maximum is observed at the same voltage (–0.7 V). Figure 9 shows the dependences of the capacitance and conductance of the *nBn* structure measured at a temperature of 295 K in the dark and when illuminated by radiation with a wavelength of 0.94 μm. It is seen that lighting leads to an increase in the amplitude of the maximum. When the structures are cooled, the maximum

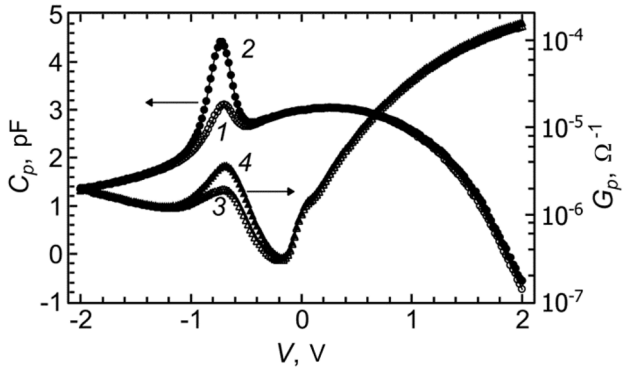

Fig. 9

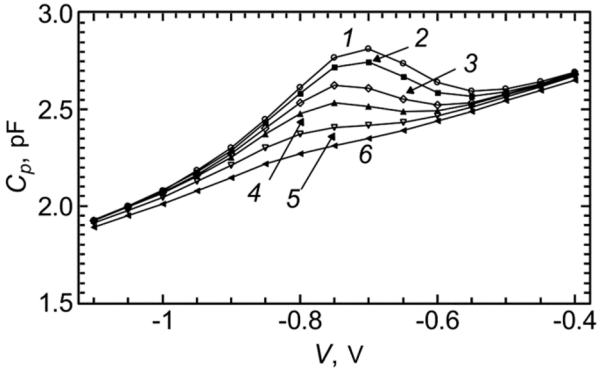

Fig. 10

Fig. 9. Voltage dependences of the capacitance (*1*, *2*) and conductance (*3*, *4*) of the *nBn* structure measured at a temperature of 295 K and a frequency of 50 kHz in the dark (*1*, *3*) and under illumination (*2*, *4*).

Fig. 10. Fragments of the C–V characteristics of the *nBn* structure measured in the dark mode at a temperature of 295 K at various frequencies, kHz: 50 (*1*), 100 (*2*), 200 (*3*), 300 (*4*), 500 (*5*), and 800 (*6*).

disappears, but under the influence of illumination, this feature can be observed in the electrophysical characteristics even at 180 K. Figure 10 shows the fragments of the C–V characteristics near the maximum measured at different frequencies. As the frequency increases, the amplitude of the maximum in the C–V characteristic decreases. The maximum in the voltage dependence of the conductance is more pronounced at high frequencies.

Most likely, the high-temperature maxima in the voltage dependences of the capacitance and conductance are due to the recharging of defect levels at the interface between the barrier and absorbing layers. With increasing frequency or with cooling, the level recharge time increases and the charge state of this level does not have time to change when the alternating test signal changes. When illuminated, the recharge time decreases and the maximum is more pronounced in the measured dependences of admittance.

At voltages close to zero, the barrier layer is completely depleted and the space charge region in the absorbing or contact layers has a minimum thickness or is absent [29]. With an increase in the reverse bias, the SCR propagates into the absorbing layer, which leads to a decrease in the measured capacitance of the *nBn* structure. In this case, the equivalent circuit shown in the inset in Fig. 11 on the right can be used. In this circuit, the capacitance C_1 characterizes the properties of the barrier layer, and the influence of the barrier resistance R_1 can be neglected in a wide range of conditions. The SCR properties in the absorbing layer can be described by the capacitance C_{abs} and the R_{SS}–C_{SS} chain, which reflects the presence of surface states (similarly to [25]). The resistance R_2 characterizes the properties of the quasi-neutral bulk of the absorbing layer. If we replace the C_{abs}, R_{SS}, and C_{SS} elements with the parallel chain C_3 and R_3 (the inset in Fig. 11 on the left), we can write the following expressions:

$$C_3 = \frac{C_{SS}}{1+\omega^2 C_{SS}^2 R_{SS}^2} + C_{abs} = \frac{C_{SS}}{1+\omega^2 \tau_{SS}^2} + C_{abs}, \quad \frac{G_3}{\omega} = \frac{1}{\omega R_3} = \frac{\omega C_{SS}^2 R_{SS}}{1+\omega^2 C_{SS}^2 R_{SS}^2} = \frac{\omega C_{SS} \tau_{SS}}{1+\omega^2 \tau_{SS}^2}, \tag{4}$$

where $\tau_{SS} = C_{SS} R_{SS}$. It follows from expression (4) that when the condition $\omega\tau_{SS} = 1$ is fulfilled, the frequency dependence $\frac{G_3(\omega)}{\omega}$ has a maximum that is observed in the experiment. Figure 11 shows the temperature dependences

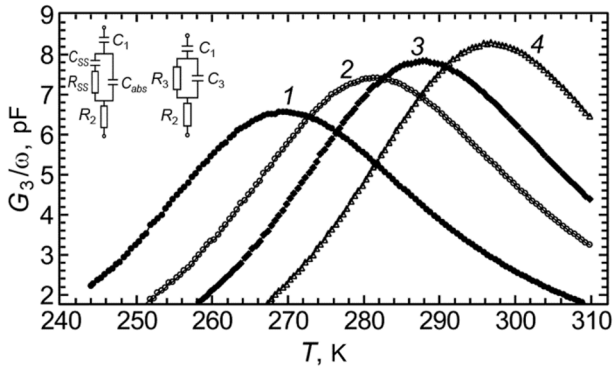

Fig. 11

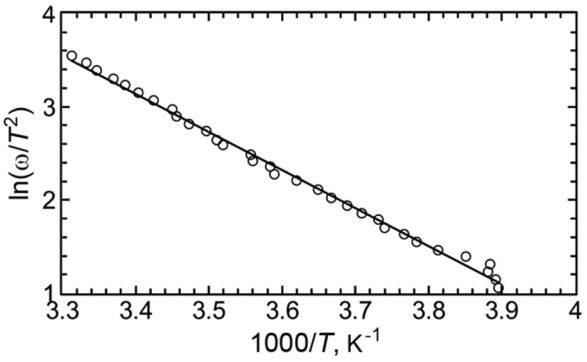

Fig. 12

Fig. 11. Temperature dependences of the normalized conductance of the depletion region of the absorbing layer G_3 measured at a voltage of –0.7 V at frequencies, kHz: 74 (*1*), 50 (*2*), 220 (*3*), and 380 (*4*). The inset shows the equivalent circuits of the *nBn* structure at reverse biases.

Fig. 12. Arrhenius plot constructed at a voltage of –0.7 V based on the temperature dependences of the normalized conductance of the absorbing layer of the *nBn* structure (Fig. 11).

of the normalized conductance of the absorbing layer SCR at various frequencies. To determine the values of $\frac{G_3}{\omega}$ from the measured impedance of the *nBn* structure, it is necessary to exclude the impedance of the barrier layer and quasi-neutral region of the absorbing layer. The values of the R_1 and R_2 elements were found from the measurements of the frequency dependences of the admittance at a voltage of 0.3 V. Figure 11 shows that the temperature dependences of the conductance have a maximum, which shifts to a higher temperature region with increasing frequency. This type of the frequency dependence can be associated with the recharging of surface states or deep levels, but the recharging of a deep level does not lead to the appearance of maxima in the voltage dependences of the capacitance and conductance [25]. Figure 12 shows the Arrhenius plot constructed at a voltage of –0.7 V. The activation energy is (359 ± 9) meV, which is possible if the surface states are located at the heterointerface between the barrier and the absorbing layer.

Admittance of MIS devices based on MBE HgCdTe *nBn* structures

Some electrophysical properties of planar MIS devices based on MBE HgCdTe *nBn* structures were studied in [33]. When a backward electrode is applied to the contact layer of an *nBn* structure, the admittance of the MIS device is determined by the contact layer properties. The measurements of C – V characteristics of planar MIS devices provide information on the properties of the HgCdTe – PE ALD Al_2O_3 interface (density of slow and fast states, fixed charge) and the near-surface MBE HgCdTe layer (impurity concentration, generation rate of minority charge carriers). In this paper, the main attention is paid to studies of the admittance of mesa MIS devices in which a backward electrode is deposited on the absorbing layer of the *nBn* structure.

Figure 13 shows the C–V characteristics of a mesa MIS device based on the *nBn* structure measured at a frequency of 10 kHz at different temperatures. Figure 13 demonstrates that at a temperature of 295 K a low-frequency C–V characteristic is realized, and at a temperature of 10 K, the behavior of the capacitance dependences is close to the high-frequency one. Upon cooling from 295 to 10 K, a significant decrease in the capacitance of the MIS device was observed in different modes. For example, in the accumulation mode, the capacitance of the MIS device decreased from 33 to 15 pF. This feature is not typical for the planar MIS devices [33], in which a backward electrode is deposited on

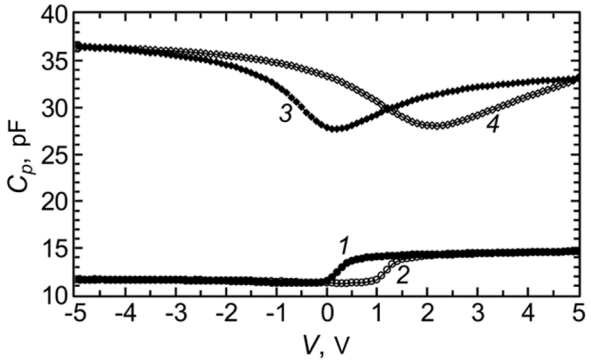

Fig. 13

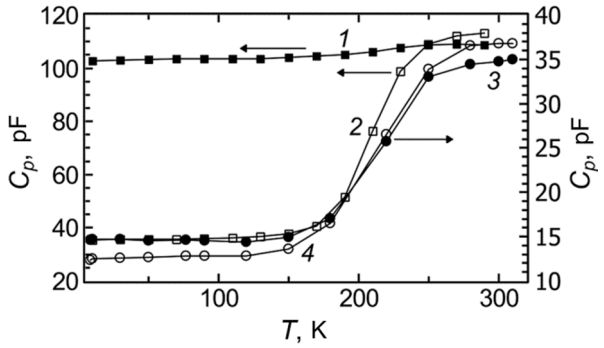

Fig. 14

Fig. 13. C–V characteristics of a mesa MIS device based on the *nBn* structure measured at a frequency of 10 kHz at a forward (*1*, *3*) and reverse (*2*, *4*) voltage scans at different temperatures, K: 10 (*1*, *2*) and 295 (*3*, *4*).

Fig. 14. Temperature dependences of the capacitance of MIS devices in a planar configuration (*1*, *2*) and mesa configuration (*3*, *4*) measured at a frequency of 10 kHz in the accumulation (*1*, *3*) and strong inversion (*2*, *4*) modes.

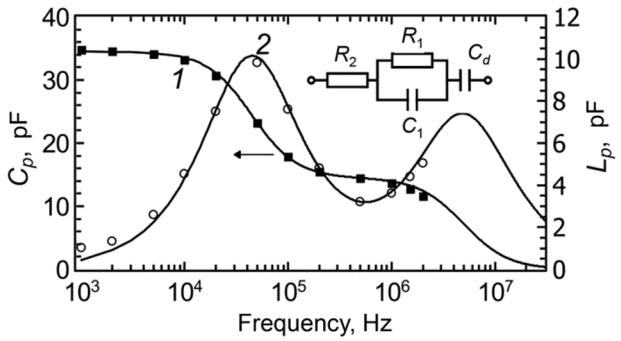

Fig. 15. Experimental and calculated frequency dependences of the capacitance (*1*) and normalized conductance (*2*) of the MIS device based on the *nBn* structure measured in the accumulation mode at a temperature of 250 K.

the contact layer. Figure 14 shows the temperature dependences of the capacitances of MIS devices in planar and mesa configurations measured in the accumulation and strong inversion modes.

It can be seen from Fig. 14 that for the planar MIS device, the accumulation capacitance is weakly dependent on temperature, and for the MIS device in the mesa configuration, the capacitance decreases significantly when cooled from 250 to 150 K. The temperature dependence of the capacitance in strong inversion for a planar MIS device is determined by the transition of the C–V characteristic from the low-frequency behavior to a high-frequency one upon cooling.

In Fig. 15, symbols show the experimental frequency dependences of the capacitance and normalized conductance of the MIS device measured in the accumulation mode at a temperature of 250 K. To calculate the frequency dependences, we used the equivalent circuit shown in the inset in Fig. 15. In this circuit, C_d is the capacitance of the insulator PE ALD Al_2O_3 layer, and the remaining designations are similar to those in the inset in Fig. 4: R_2 is the series resistance of the bulk of the absorbing MBE HgCdTe layer, R_1 and C_1 are the resistance and capacitance of the

barrier layer, respectively. To describe the properties of the mesa MIS device in the depletion or inversion modes, a more complex equivalent circuit is needed that takes into account processes in the near-surface region of the contact layer.

A parallel chain of R_1 and C_1characterizing the barrier layer properties can be converted into a series chain of R_{1s} and C_{1s} using the following relations:

$$R_{1s} = \frac{R_1}{1+\omega^2 C_1^2 R_1^2},\ C_{1s} = \frac{1+\omega^2 C_1^2 R_1^2}{\omega^2 C_1 R_1^2}. \tag{5}$$

If we represent a MIS device in the form of the series connected capacitance C_s and resistance R_s, we can write

$$C_s = \left(\frac{1}{C_d} + \frac{1}{\tilde{N}_{1s}}\right)^{-1},\ R_s = R_2 + R_{1s}. \tag{6}$$

Then, the measured capacitance and conductance of the MIS device for a parallel equivalent circuit will be equal to

$$C_p = \frac{C_s}{1+\omega^2 C_s^2 R_s^2},\ G_p = \frac{\omega^2 C_s^2 R_s}{1+\omega^2 C_s^2 R_s^2}. \tag{7}$$

The measured values of the capacitance and conductance of the MIS device in the mesa configuration can be written taking into account the values of the equivalent circuit elements in the following form:

$$C_p = \frac{\left(\frac{C_d\left(1+\omega^2\tau_1^2\right)}{1+\omega^2\left(C_d+C_1\right)C_1R_1^2}\right)}{1+\omega^2\left(R_2+\frac{R_1}{1+\omega^2\tau_1^2}\right)^2\left(\frac{C_d\left(1+\omega^2\tau_1^2\right)}{1+\omega^2\left(C_d+C_1\right)C_1R_1^2}\right)^2}, \tag{8}$$

$$G_p = \frac{\omega^2\left(R_2+\frac{R_1}{1+\omega^2\tau_1^2}\right)\left(\frac{C_d\left(1+\omega^2\tau_1^2\right)}{1+\omega^2\left(C_d+C_1\right)C_1R_1^2}\right)^2}{1+\omega^2\left(R_2+\frac{R_1}{1+\omega^2\tau_1^2}\right)^2\left(\frac{C_d\left(1+\omega^2\tau_1^2\right)}{1+\omega^2\left(C_d+C_1\right)C_1R_1^2}\right)^2}, \tag{9}$$

where $\tau_1 = R_1C_1$.

From the results of measuring the frequency dependences of the MIS device capacitance and conductance in the accumulation mode, it is easy to determine the values of all elements of the equivalent circuit. The low-frequency capacitance of the MIS structure is close to the capacitance of the insulator. The value of the barrier layer capacitance C_1 strongly affects the measured capacitance at frequencies corresponding to the gently sloping part of the C–V characteristic (in the frequency range from 200 to 1000 kHz). The resistance R_1 can be found by the frequency corresponding to the maximum of the normalized conductance, and the resistance R_2 can be found by the high-frequency decay of the frequency dependence of the capacitance or by the high-frequency maximum of the normalized

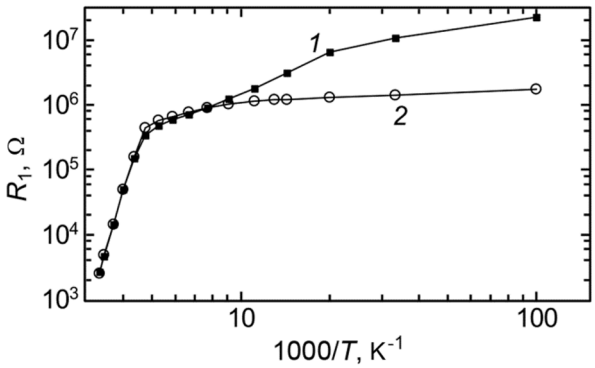

Fig. 16. Dependences of the barrier layer resistance of the MIS device based on the *nBn* structure obtained from the admittance measurements in the dark mode (*1*) and under illumination (*2*).

conductance. The calculated frequency dependences of the capacitance and conductance of the MIS device are shown with lines in Fig. 15. The following values of the equivalent circuit elements were used in the calculation: C_d = 34.5 pF, R_1 = 58.6 kΩ, C_1 = 26.1 pF, and R_2 = 2.2 kΩ. These values of the equivalent circuit elements (R_1, C_1, R_2) slightly differ from the values obtained from the frequency dependences of the *nBn* structure admittance, which is associated with different areas of the front electrodes for the *nBn* structure (Fig. 4) and the MIS device (Fig. 15).

Taking into account expressions (5)–(9), it is easy to obtain relations that allow one to exclude the influence of the barrier and absorbing layers parameters on the measured admittance of the mesa MIS device. Such a procedure can be used to diagnose the properties of the interface and near-surface region of the contact layer. A comparison of the experimental frequency dependences with the results of numerical modeling (using relations (5)–(9)) allows finding the values of the elements characterizing the barrier layer under various conditions. For example, Fig. 16 shows the temperature dependences of the barrier layer resistance R_1 found in the dark and when illuminated by radiation with a wavelength of 0.94 μm. Figure 16 shows that infrared illumination leads to a decrease in the values of the resistance R_1 at low temperatures (<100 K). The activation energies found according to the dependences in Fig. 16, were 346 and 16 meV in the region of a high-temperature drop of the resistance and at lower temperatures, respectively. The obtained activation energy values can be explained by the fact that, at high temperatures, the resistance R_1 is limited by the Shockley–Read generation processes, and at low temperatures, by tunneling generation processes via a level in the band gap.

CONCLUSIONS

Thus, in a wide range of frequencies and temperatures, the dependences of the admittance for *nBn* structures based on MBE HgCdTe were studied. For the structures under study at temperatures from 180 to 300 K, the dark current is limited by the diffusion processes. An equivalent circuit is proposed that allows one to calculate the frequency dependences of the admittance of *nBn* structures based on MBE HgCdTe at voltages close to zero. The proposed circuit contains the parallel connected capacitance and resistance of the barrier, as well as a series resistance of the absorbing layer bulk. It was found that at temperatures lower than 220 K, the influence of the barrier layer resistance can be neglected in a wide frequency range (1–2000 kHz). It is shown that the measurements of C–V characteristics of *nBn* structures based on MBE HgCdTe can be used in a wide range of frequencies and temperatures to determine the dopant concentration in the absorbing layer.

At temperatures close to room temperature, in order to correctly describe the dependences of admittance, it is necessary to use a more complex equivalent circuit due to the influence on the measurement results of the features of real *nBn* structures based on MBE HgCdTe. These features include the presence of surface states at the heterointerface,

the frequency dispersion of the C–V characteristics, and negative capacitance values at forward biases. The activation energy of the discrete level of surface states, determined from the Arrhenius plot, was about 359 meV, which confirms the assumption about the location of surface states at the interface between the barrier and the absorbing layer. The admittance of MIS devices based on *nBn* structures was studied when a backward electrode was deposited on the absorbing layer (mesa configuration). It is shown that the electrophysical characteristics of the MIS device in the mesa configuration are determined by the combined influence of processes in the contact, barrier, and absorbing layers of the *nBn* structure. The admittance measurements of MIS devices in the mesa configuration can be used to diagnose the properties of the near-surface region of the contact layer and the Al_2O_3 – HgCdTe interface, as well as to study the processes in the barrier layer.

The research was supported by a grant from the Russian Science Foundation (project No. 19-12-00135).

REFERENCES

1. A. Rogalski, Infrared and Terahertz detectors, 3rd. ed., Boca Raton: CRC Press, Taylor & Francis Group (2019).
2. M. A. Kinch, State-of-the-Art Infrared Detector Technology, SPIE Press, Bellingham, Washington (2014).
3. C. Lobre, P. H. Jouneau, L. Mollard, *et al*., J. Electron. Mater., **43**, 2908–2914 (2014).
4. I. I. Izhnin, K. D. Mynbaev, A. V. Voitsekhovsky, *et al*., Infrared Phys. Technol., **98**, 230–235 (2019).
5. A. M. White, Infrared Detectors, U.S. Patent 4697063 (1983).
6. P. Klipstein, Depletion-Less Photodiode with Suppressed Dark Current and Method for Producing the Same, U.S. Patent 7795640 (2003).
7. S. Maimon and G. W. Wicks, Appl. Phys. Lett., **89**, No. 15, 151109 (2006).
8. D. Z. Ting, A. Soibel, A. Khoshakhlagh, *et al*., Appl. Phys. Lett., **113**, 021101 (2018).
9. A. Soibel, D. Z. Ting, C. J. Hill, *et al*., Appl. Phys. Lett., **109**, 103505 (2016).
10. A. Evirgen, J. Abautret, J. P. Perez, *et al*., Electron. Lett., **50,** 1472–1473 (2014).
11. A. Soibel, D. Z. Ting, S. B. Rafol, *et al*., Appl. Phys. Lett., **114**, 161103 (2019).
12. N. D. Akhavan, G. A. Umana-Membreno, R. Gu, *et al*., IEEE Trans. Electron Dev., **63**, No. 12, 4811–4818 (2016).
13. M. Kopytko, J. Wróbel, K. Jóźwikowski, *et al*., J. Electron. Mater., **44**, No. 1, 158–166 (2015).
14. F. Uzgur and S. Kocaman, Infrared Phys. Technol., **97**, 123–128 (2019).
15. Z. H. Ye, Y. Y. Chen, P. Zhang, *et al*., Proc. SPIE, **9070**, 90701L (2014).
16. A. M. Itsuno, J. D. Phillips, and S. Velicu, J. Electron. Mater., **40**, No. 8, 1624–1629 (2011).
17. P. Martyniuk, M. Kopytko, and A. Rogalski, Opto-Electron. Rev., **22**, No. 2, 127–146 (2014).
18. A. M. Itsuno, J. D. Phillips, and S. Velicu, Appl. Phys. Lett., **100**, No. 16, 161102 (2012).
19. S. Velicu, J. Zhao, M. Morley, *et al*., Proc. SPIE, **8268**, 826282X (2012).
20. O. Gravrand, F. Boulard, A. Ferron, *et al*., J. Electron. Mater., **44**, No. 9, 3069–3075 (2015).
21. M. Kopytko, A. Kębłowski, W. Gawron, *et al*., IEEE Trans. Electron Dev., **61**, No. 11, 3803–3807 (2014).
22. M. Kopytko and A. Rogalski, Prog. Quant. Electron., **47**, 1–18 (2016).
23. A. V. Voitsekhovskii, S. N. Nesmelov, S. M. Dzyadukh, *et al*., Infrared Phys. Technol., **102**, 103035 (2019).
24. A. V. Voitsekhovskii, S. N. Nesmelov, S. M. Dzyadukh, *et al*., J. Phys. D: Appl. Phys., **53**, No. 5, 055107 (2020).
25. E. H. Nicollian and J. R. Brews, MOS (Metal Oxide Semiconductor) Physics and Technology, Wiley, N. Y. (1982).
26. S. M. Sze and K. Ng Kwok, Physics of Semiconductor Devices, 3rd ed., Wiley, N. Y. (2007).
27. A. V. Voitsekhovskii, S. N. Nesmelov, and S. M. Dzyadukh, J. Phys. Chem. Sol., **102**, 42–48 (2017).
28. H. Hirwa, S. Pittner, and V. Wagner, Org. Electron., **24**, 303–314 (2015).
29. D. R. Rhiger, E. P. Smith, B. P. Kolasa, *et al*., J. Electron. Mater., **45**, No. 9, 4646–4653 (2016).
30. A. Glasmann, I. Prigozhin, and E. Bellotti, IEEE J. Electron Dev. Soc., **7**, 534– 543 (2019).

31. A. V. Voitsekhovskii, S. N. Nesmelov, and S. M. Dzyadukh, *et al*., Mater. Res. Expr., **6**, No. 11, 116411 (2019).
32. A. V. Voitsekhovskii, S. N. Nesmelov, and S. M. Dzyadukh, *et al*., Russ. Phys. J., **62**, No. 5, 818-826 (2019).
33. A. V. Voitsekhovskii, S. N. Nesmelov, and S. M. Dzyadukh, *et al*., J. Comm. Technol. Electron., **64**, No. 3, 289–293 (2019).
34. R. Fu and J. Pattison, Opt. Eng., **51**, No. 10, 104003 (2012).
35. E. R. Zakirov, V. G. Kesler, G. Y. Sidorov, *et al*., Semicond. Sci. Technol., **34**, No. 6, 065007 (2019).
36. M. Ershov, H. C. Liu, L. Li, *et al*., IEEE Trans. Electron. Dev., **45**, No. 10, 2196–2206 (1998).
37. B. K. Jones, J. Santana, M. McPherson, *et al*., Sol. State Commun., **107**, No. 2, 47–50 (1998).
38. N. A. Penin, Semiconductors, **30**, No. 4, 340–343 (1996).
39. A. V. Voitsekhovskii, S. N. Nesmelov, and S. M. Dzyadukh, *et al*., Russ. Phys. J., **57**, No. 4, 536–544 (2014).
40. A. V. Voitsekhovskii, S. N. Nesmelov, and S. M. Dzyadukh, *et al*., Russ. Phys. J., **57**, No. 5, 633–641 (2014).
41. A. V. Voitsekhovskii, S. N. Nesmelov, and S. M. Dzyadukh, *et al*., Infrared Phys. Technol., **71**, 236–241 (2015).
42. W. Van Gelder and E. H. Nicollian, J. Electrochem. Soc., **118**, 138–141 (1971).